Nuclear Instruments and Methods 216 (1983) 329–348
North-Holland Publishing Company

ON THE COMPUTATION OF RESONANT MODES IN CYLINDRICALLY SYMMETRIC CAVITIES

T. WEILAND

Deutsches Elektronensynchrotron, DESY, Notkestr. 85, 2000 Hamburg, FRG

Received 7 February 1983

Intense bunches of charged particles in accelerators excite transverse higher modes in accelerating cavities. These higher modes lead to an interaction between widely seperated bunches. Such multi-bunch or multi-turn instabilities due to long range forces can be described by the cavity mode frequencies and field patterns. For structures of cylindrical symmetry a computer code named URMEL is described which calculates resonant modes of any azimuthal mode number $m = 0, 1, 2 \ldots$ (monopole, dipole, quadrupole, etc.). The eigenfrequencies are found as linear eigenvalues of a large matrix and simple mathematical procedures guarantee that no modes are missed. The combined use of URMEL in the frequency domain and of the complementary code TBCI in the time domain enables a complete analysis of long range – low frequency – forces (narrow band impedances) and short range – high frequency – forces (broad band impedances).

1. Preface

Hollow metallic structures – called cavities – serve as a means to keep electromagnetic energy confined to a finite volume. In accelerator technology such cavities are mainly used to accelerate or deflect particles by means of resonant modes excited by external power sources. In order to evaluate quantitatively the frequencies, quality factors and coupling coefficients for the resonant eigenmodes, several computer codes have been developed in the last two decades. In order to enable calculations with arbitrarily shaped cavities these codes are based on "mesh methods". There are three main groups of cavities: fully three dimensional structures, cavities with a constant cross section and structures of cylindrical symmetry.

One of the first computer codes for *three dimensional* resonators was published by Albani and Bernardi in 1974 [1]. Their method included dielectric blocks inside the cavities. The most recent program of this kind was written by Wilhelm [2] in 1982. The computational problem of three dimensional cavities is that the calculations need an enormous amount of time. Furthermore, most of the cavities used in practice have some kind of symmetry which eases the calculations significantly. So far three dimensional codes are not (yet) commonly used.

The second group of cavities are those with a *constant cross section*, i.e. cavities the shape of which does not change along one cartesian dimension. In this case one can separate one coordinate in Maxwell's equations and by doing this reduce the three dimensional problem to a quasi-two dimensional one. Structures of constant cross section are used in rf technology as waveguides. There are too many papers about such codes to list them all here. The first codes were made for empty two dimensional cavities such as hollow waveguides and coaxial cables. The more complicated problem with a material inside the cross section was solved next with applications to microstrip techniques and optical fiber technology [3–5]. A rather sophisticated code of this type has been published by the author in 1979 [5]. This program solves the most general case with arbitrarily shaped blocks of lossy anisotropic material (tensorial permeability, complex permittivity and conductivity) and computes frequencies and damping rates. The most recent code for constant cross section cavities is also described in ref. 2.

Most cavities used in accelerator technology are of *cylindrical symmetry*. As a consequence the fields of the resonant modes are cylindrically symmetric and the azimuthal dependence can be taken out analytically from the numerical computation. Modes can thus be grouped according to the azimuthal dependence, $\cos m\varphi$, of the fields. Fields with $m = 0$ are used to accelerate particles. Higher modes with $m > 0$ are called

deflecting or transverse modes. Several computer codes have been written for the evaluation of modes with $m = 0$, e.g. [7–9], the best known of which is probably SUPERFISH by Halbach and Holsinger. Recently improved versions have been described by Fomel et al. [10] and Fernandes et al. [11]. Since fields with $m > 0$ invoke all six field components in Maxwell's equations, computer codes for these bear many computational problems. This paper deals with the computation of modes for any azimuthal mode number m in structures of cylindrical symmetry – which are in fact the most important ones in present accelerator technology.

2. Introduction

Deflecting resonant modes in accelerating cavities of cylindrical symmetry are excited by off-axis bunches of charged particles. Modes with high quality factors lead to so called long range forces which carry the interaction between different bunches which may be far apart from each other. In storage rings a bunch may interact with its own fields after one turn and suffer from multi-turn instabilities or many bunches may generate multi-bunch instabilities. Even in large storage rings such forces become important when superconducting cavities are used since their memory is certainly longer than the revolution time of any realistic ring.

The knowledge of the full mode structure of an accelerating cavity is very important for many design considerations and for stability cures such as mode damping antennae. Since most of the cavities used in practice are of rather complicated shape any analytical ansatz will fail. The only known way to analyze arbitrarily shaped geometries is by mesh methods.

The first code for transverse cavity modes named TRANSVRS [12] is restricted to an infinite chain of pill-box cavities with connecting beam tubes and is an extension of the code KN7C [13]. Recently two programs have been described that can deal with realistically shaped cavities by means of a triangular mesh method [14,15]. Both methods transform Maxwell's equations into a nonlinear eigenvalue problem for a large matrix. The use of both the azimuthal field components E_φ and H_φ together with a triangular mesh causes a serious problem: elements of the matrix have poles given by the eigenfrequencies and as a consequence the condition number of the matrix is decreased. Numerical problems occur and the use of such a code for many modes becomes laborious [16]. Apart from this *intrinsic* difficulty the matrix eigenvalue problem is in addition *nonlinear*.

The mathematical ansatz used for the program described in this paper is based on the FIT-method [17] which has been successfully applied to similar problems in the past [6,9,18]. The method uses a rectangular mesh in which each rectangle can be further subdivided into triangles. This kind of mesh in many cases enables very good approximations of odd shaped structures to be made almost as good as those obtained with fully triangular meshes. One of the main advantages of this method is that it always yields a *linear* matrix eigenvalue problem the eigenvalue of which is the wave number squared. This is achieved by using the components E_r and E_z of the electric field. For the special case of azimuthally independent fields the code uses (similiarly to others [7–11]) the azimuthal magnetic field component H_φ with a special weight chosen such that the resulting matrix becomes fully symmetric. The fact that the eigenvalue problem is *linear* in both cases enables the application of simple numerical methods for the eigenvalue computation to be made. Eigenvectors and eigenfrequencies are found by vector iteration combined with a spectral shift. Solutions are found in ascending order of frequency.

The computer code URMEL is written in FORTRAN IV and freely available. Typical cpu time is of the order of three minutes per deflecting mode for a mesh of 1000 nodes on an IBM3081. Monopole modes need only a small fraction of this time. Graphical output of the magnetic and electric fields may be obtained as well as all the usual printout of field components, quality factors and shunt impedances. The input data are kept as similar as possible to the TBCI [18] conventions is order to ease the combined use of these two complementary cavity codes. A separate user guide [19] for URMEL is available with instructions for installation and test examples.

The symbols used in this article are listed at the end of the appendix.

3. Discretization

Electromagnetic fields in geometries of cylindrical symmetry having an harmonic time dependence can be written generally as:

$$\boldsymbol{E}(r, \varphi, z, t) = \sqrt{Z_0}\ \sin \omega t \cdot \sum_m \{\boldsymbol{e}_r E_{m,r}(r, z) \cos m\varphi + \boldsymbol{e}_\varphi E_{m,\varphi}(r, z) \sin m\varphi + \boldsymbol{e}_z E_{m,z}(r, z) \cos m\varphi\} \tag{1}$$

$$\boldsymbol{H}(r, \varphi, z, t) = \sqrt{Y_0}\ \cos \omega t \cdot \sum_m \{\boldsymbol{e}_r H_{m,r}(r, z) \sin m\varphi + \boldsymbol{e}_\varphi H_{m,\varphi}(r, z) \cos m\varphi + \boldsymbol{e}_z H_{m,z}(r, z) \sin m\varphi\} \tag{2}$$

Leaving out the time dependent factors the normalizations as well as the azimuthal mode number m, Maxwell equations read for each azimuthal subset m as:

$$\text{rot } \boldsymbol{E} = k\boldsymbol{H}, \qquad \text{rot } \boldsymbol{H} = k\boldsymbol{E}, \qquad k = \omega/c \tag{3}$$

$$\text{div } \boldsymbol{E} = 0, \qquad \text{div } \boldsymbol{B} = 0. \tag{4}$$

In the following the azimuthal mode number m will be omitted. Fig. 1a shows a realistic shape of an accelerating cavity as used in PETRA. In order to solve the above equations for such an arbitrarily shaped structure a grid will be used in which only one half of the upper part in fig. 1a is necessary due to symmetry. This is indicated in fig. 1b. The step sizes in r and z direction may vary and each rectangle may be further subdivided into triangles for better approximation of odd shaped cavities as shown in fig. 2. The unknown functions representing all the field components $E_{r,\varphi,z}$ and $H_{r,\varphi,z}$ are replaced by their values at a finite number of different locations in the grid. Fig. 3 shows the locations and also the convention of counting the grid nodes and field components.

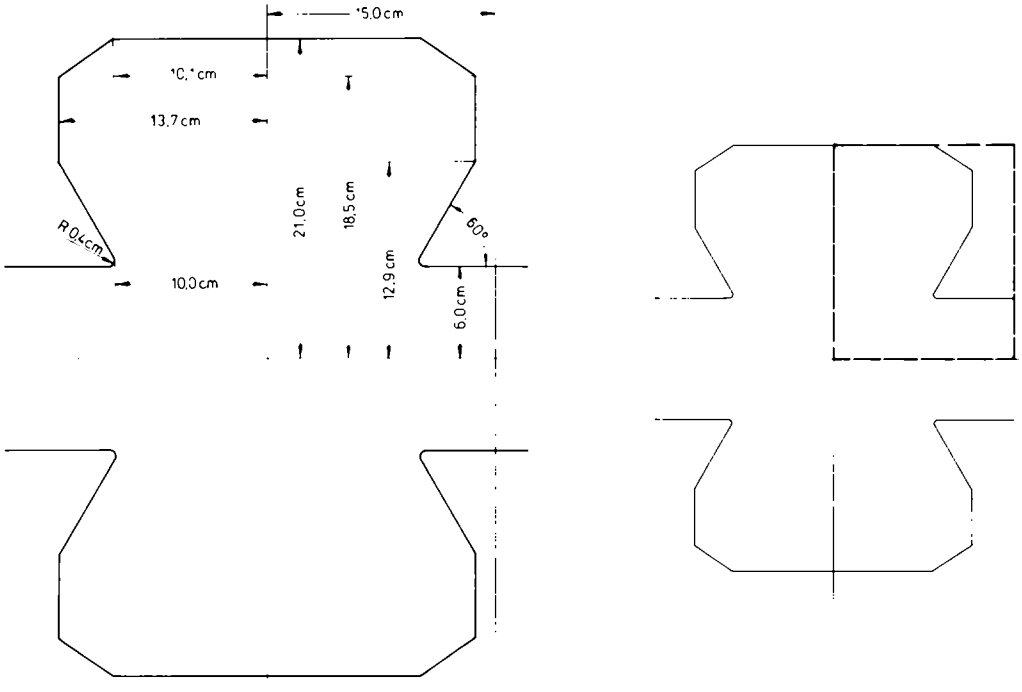

Fig. 1. Shape of the PETRA accelerating cavity (The part needed for the representation in the mesh is indicated by the dashed lines.)

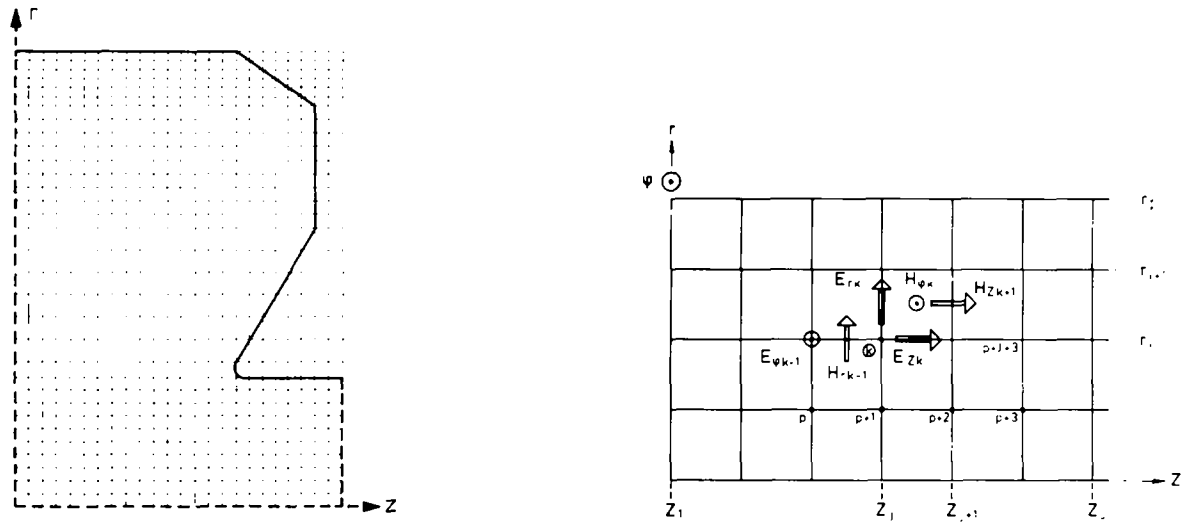

Fig. 2. Rectangular mesh with varying step size and the right half of the PETRA accelerating cavity.

Fig. 3. Mesh in the (r, z) plane and locations of unknown field components. Mesh points are numbered first in z direction then in r direction. The global number of mesh node k is $k = (i-1)\cdot I + j$.

Certainly one does not need to solve the eigenvalue problem of eq. (3) for all six field components. Depending on whether we have $m = 0$ (monopole modes) or $m > 0$ (deflecting transverse modes) different schemes apply.

3.1. Deflecting transverse modes ($m > 0$)

There are several ways to eliminate four components of $\boldsymbol{E}$ and $\boldsymbol{H}$ in eq. (3) so that only two remain. As mentioned in the introduction we will use the radial and longitudinal electric field components. This subset yields a *linear* algebraic eigenvalue problem and does not cause problematic poles as does the choice of both azimuthal components [14,15]. The details of the derivations are given in the appendix. Solving Maxwells equations in integral form up to first order approximation finally yields a linear relation between a field component and eight neighbours:

$$k^2 E_{r,k} = a_{rr,k,0}E_{r,k} - a_{rr,k,1}E_{r,k-J} - a_{rr,k,2}E_{r,k-1} - a_{rr,k,3}E_{r,k+1} - a_{rr,k,4}E_{r,k+J} - a_{rz,k,1}E_{z,k-1} - a_{rz,k,2}E_{z,k} - a_{rz,k,3}E_{z,k+J-1} - a_{rz,k,4}E_{z,k+J} \tag{5}$$

$$k^2 E_{z,k} = a_{zz,k,0}E_{z,k} - a_{zz,k,1}E_{z,k-J} - a_{zz,k,2}E_{z,k-1} - a_{zz,k,3}E_{z,k+1} - a_{zz,k,4}E_{z,k+J} - a_{zr,k,1}E_{r,k-J} - a_{zr,k,2}E_{r,k-J+1} - a_{zr,k,3}E_{r,k} - a_{zr,k,4}E_{r,k+1}. \tag{6}$$

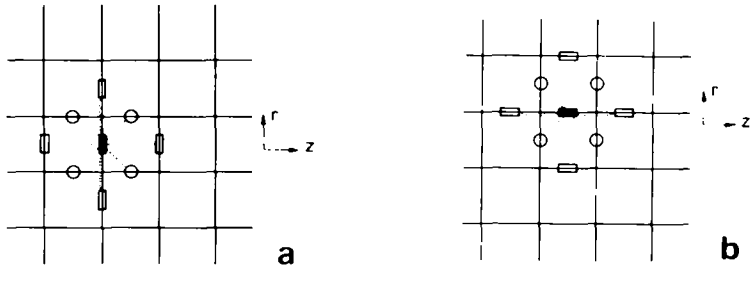

Fig. 4. Schematical representation of difference operators relating eight neighbouring field components to the central one.

Equations such as these exist for each point in the mesh and are called "difference operator equations". Fig. 4 shows schematically the local connections of these difference operators in the grid. The explicit form of the operator coefficients in (5) and (6) is much too complicated to be given here since there exist 15625 different forms of (5) and (6). It is shown in the appendix how this enormous variety of equations can be reduced to a combined solution of only a few sub-operators. The sub-operators are basically solvers for the single components of Maxwell's equations written as the two vector equations (3) and (4). The many possibilities can be reduced to rather basic logical decisions and the computer code actually constructs the above equations out of many formal sub-equations in a quasi analytical manner.

Once all the equations of type (5) and (6) are set up, all together form a linear algebraic eigenvalue problem:

$$\begin{pmatrix} A_{rr} & A_{rz} \\ A_{zr} & A_{zz} \end{pmatrix} \boldsymbol{e} = k^2 \boldsymbol{e}. \tag{7}$$

The submatrices indicate that the matrix is blocked. The upper row represents eq. (5) at all mesh points, the second row eq. (6). $\boldsymbol{e}$ represents a column vector holding all the unknown field components:

$$\boldsymbol{e} = (E_{r,1}, E_{r,2}, \ldots, E_{r,N-1}, E_{r,N}, E_{z,1}, E_{z,2}, \ldots, E_{z,N-1}, E_{z,N})^t. \tag{8}$$

The matrix is of sparse type. The structure of the matrix is schematically shown in fig. 5. As can be seen in eqs. (5) and (6) – which are nothing but formal rows of the matrix – the matrix has only nine bands. The submatrices A_{rr} and A_{zz} can be transformed into symmetric matrices by using a diagonal matrix transformation. The physical interpretation of this transformation is that instead of the field components one uses the square root of the energy density due to the field component. In the radial case the density is furthermore multiplied with the radius r:

$$E_r \to E_r \cdot r \cdot \sqrt{\mathrm{d}r \cdot r\mathrm{d}\varphi \cdot \mathrm{d}z} \tag{9}$$

$$E_z \to E_z \cdot \sqrt{\mathrm{d}r \cdot r\mathrm{d}\varphi \cdot \mathrm{d}z}\,. \tag{10}$$

The new variables have symmetric submatrices A_{rr} and A_{zz} requiring less storage locations than asymmetric ones. Unfortunately there exists no such simple transformation that makes the entire matrix symmetric.

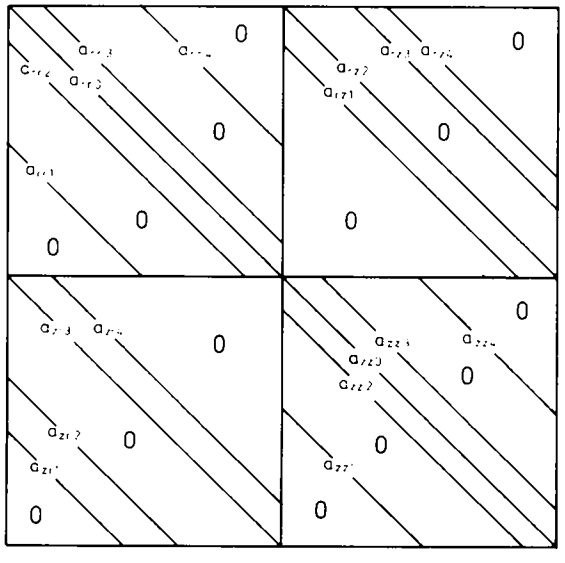

Fig. 5. Schematical structure of the matrix for transverse modes with 9 bands. Outside the bands are zeros.

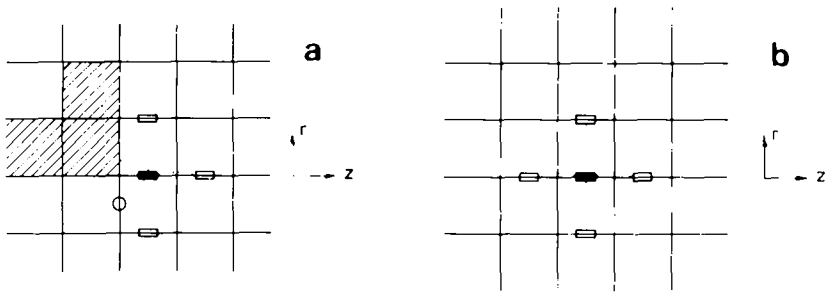

Fig. 6. (a) Difference operator near a boundary which is not parallel to r on to z. Only nonzero coupling elements are shown. (b) Difference operator for the z component of the electric field away from any boundary showing no arms to radial components.

Why this is so can be found only by carefully inspecting the coupling coefficients between E_r and E_z in (5) and (6). It is found that all the elements of A_{rz} are nonzero but most of the elements of A_{zr} vanish. Actually one finds nonzero coefficients only near a boundary and only if the boundary surface is not parallel to r nor to z. A schematical difference operator for $\boldsymbol{E}$ in vacuum and near a boundary is shown in fig. 6. These vanishing coefficients reflect some well known physics:

In a pill box cavity TM and TE modes are decoupled. Each type of mode has only five field components and can be described mathematically by only a single scalar function – e.g. a vector potential component – or in this case by E_r(TE) or by E_z(TM). For any deviation in shape from a pill box it is well known that six field components are necessary in order to fulfill all of the four Maxwell's equations. The six field components may be split into a combination of TE and TM modes which are then coupled. This is indeed what can be found by inspecting the matrix coefficients. For a pill box the eigenvalue problem falls apart into two separate ones, each one of which has only half the order. In all other cases the full matrix problem has to be solved and it may be considered to be a coupled problem of the TE and TM mode sub matrices.

3.2. Longitudinal modes ($m = 0$)

For the solutions that do not depend on the azimuthal variable φ one is usually only interested in TM modes. These modes have only three nonzero components and the eigenvalue equations can be reduced to a single one. As usual we use the azimuthal magnetic field and get a difference operator that connects each unknown magnetic field component with four neighbours:

$$k^2 H_{\varphi,k} = a_{k,0} H_{\varphi,k} - a_{k,1} H_{\varphi,k-J} - a_{k,2} H_{\varphi,k-1} - a_{k,3} H_{\varphi,k+1} - a_{k,4} H_{\varphi,k+J}. \tag{11}$$

The schematic operator is shown in fig. 7. Writing down all the local difference equations for all points in

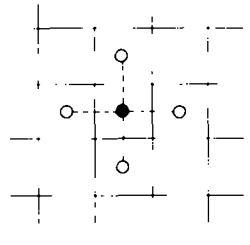

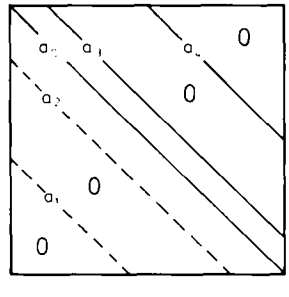

Fig. 7. Schematical difference operator with four arms to azimuthal magnetic field components as used for rotationally symmetric fields ($m = 0$).

Fig. 8. Schematical structure of the sparse matrix for longitudinal modes. Outside the bands are zeros.

the mesh finally yields again a linear algebraic eigenvalue problem:

$$\boldsymbol{A}\boldsymbol{h} = k^2\boldsymbol{h}, \tag{12}$$

$\boldsymbol{h}$ denotes a column vector holding all components of the azimuthal magnetic field:

$$\boldsymbol{h} = (H_{\varphi,1}, H_{\varphi,2}, H_{\varphi,3}, \ldots, H_{\varphi,N-1}, H_{\varphi,N})^{\mathrm{t}}. \tag{13}$$

The matrix A in (12) is not symmetric. The structure of the matrix is schematically shown in fig. 8. Using the usual [8] $r \cdot H_\varphi$ instead of H_φ does also not yield a symmetric matrix. The final choice for the diagonal transformation of A is again the square root of the energy density due to the field component. The transformation means that weighted functions are used instead of the original fields:

$$H_\varphi \to H_\varphi \sqrt{\mathrm{d}r \cdot r \mathrm{d}\varphi \cdot \mathrm{d}z}. \tag{14}$$

The final matrix is symmetric thus allowing much simpler eigenvalue procedures to be applied than for an asymmetric matrix.

4. Computation of eigenvalues

For large sparse matrices of a linear algebraic eigenvalue problem of the so called "simple type":

$$\boldsymbol{A}\boldsymbol{x} = \lambda\boldsymbol{x}, \qquad \lambda \in R, \qquad \boldsymbol{x} \in R^N, \qquad \boldsymbol{A} \in R^{N\times N}, \tag{15}$$

there exists a rather obvious way of finding the largest eigenvalue. We assume that the eigenvalues of A obey:

$$|\lambda_1| > |\lambda_2| \geqq |\lambda_3| \cdots \geqq |\lambda_N|. \tag{16}$$

Any vector decomposed into eigenvectors of A multiplied with A will increase in its content of the eigenvector belonging to the largest eigenvalue. Multiplying this result again and again with A will supress more and more all other contents. It can be shown rigorously [20] that the following sequence converges towards the largest eigenvalue λ_1:

$$\lim_{i,j\to\infty} \Lambda_{i,j} = \lim_{i,j\to\infty} \{\boldsymbol{v}_j \cdot \boldsymbol{A}\boldsymbol{u}_i / \boldsymbol{v}_j \cdot \boldsymbol{u}_i\} = \lambda_1. \tag{17}$$

In this expression the "left" and the "right" iterated vectors have to be used in case of asymmetric matrices:

$$\boldsymbol{v}^{j+1} = \boldsymbol{A}^{\mathrm{t}}\boldsymbol{v}^j \tag{18}$$

$$\boldsymbol{u}^{i+1} = \boldsymbol{A}\boldsymbol{u}^i. \tag{19}$$

The behaviour of the expression (17) is known to be of quadratic convergence with $n = i = j$:

$$\Lambda_{nn} = \lambda_1 + \mathcal{O}\{(\lambda_2/\lambda_1)^{2^n}\}. \tag{20}$$

This elegant method yields the eigenvector and the eigenvalue at the same time. There is no need to solve a linear system of equations for the calculation of the eigenvectors. Unfortunately one is usually interested in the smallest eigenvalues (which correspond to the lowest frequency) rather than in the largest one. A commonly used way is to invert the matrix before iteration since matrix inversion also inverts the eigenvalues. This scheme called "inverse iteration" destroys the band character of the matrix and fills up all the elements between the outermost bands (see figs. 5 and 8). As a consequence additional storage is needed. The additional number of storage locations can be estimated for a square mesh to be $\sqrt{N}/10$. It seems to be much easier to use a simple shift of the entire eigenvalue spectrum of the matrix such that the absolute smallest eigenvalue becomes the largest one and vice versa. An obvious choice for the amount of

the shift is λ_1. The largest eigenvalue will be turned into zero that way. Instead of the original matrix A we use:

$$B = A - \lambda_1 I \tag{21}$$

with I being a unit matrix. The new eigenvalue equation still has the same eigenvectors as the original one but the eigenvalues are shifted:

$$Bx = \mu_n x, \qquad \mu_n = \lambda_n - \lambda_1, \qquad n = 1, 2, \ldots, N. \tag{22}$$

The largest eigenvalue can be estimated by Gerschgorin circles or can be found by iteration. High accuracy is obviously not needed for λ_1.

Next higher eigenvectors are found by the same procedure with an additional operation: After each iteration the result is made orthogonal to the already known vectors. This makes the Rayleigh expression (17) converge towards the next higher eigenvector and value. The obvious advantages of this iterative eigenvalue finder are that the solutions are found in ascending order of frequency and that no solutions can be missed. Furthermore the eigenvectors and values are found at the same time. The price for these advantages is that for higher modes one has to provide all the eigenvectors found before for the orthogonalization. At some very high order this limits the number of solutions that can be found. As will be discussed later a serious limit has not yet been found and in most of commonly used cavity types one can easily compute all the modes up to the beam pipe cutoff frequency.

5. The computer code URMEL

The computer code named URMEL that verifies the theory described above is written in FORTRAN IV and a detailed user guide is available [19]. Here we will only summarize some characteristics.

- The version of URMEL being distributed needs about 200 000 computer words (corresponding to two Megabytes on IBM) and computes up to 20 transverse modes or 50 longitudinal modes. (A second version with half the core size and a maximum of five transverse/20 longitudinal modes is also available). Since most cavities are symmetric to a mid plane in the direction of the beam path the actual number of modes that can be calculated is 40 for each $m > 0$ and 100 for $m = 0$.
- The maximum number of mesh points is preset to 2000 and can easily be changed.
- Typical cpu time consumption on an IBM 3081 is of the order of three minutes per transverse mode and roughly half a minute for monopole modes in a grid of 1000 nodes.
- All fields may be printed or plotted and all shunt impedance related quantities are calculated.
- The code is extendable to dielectric and permeable insertions of any shape.
- Input data conventions are kept close to the TBCI [18] data structure in order to facilitate combined use.
- A half automatic mesh generator is available that can process elliptical and other geometries.

6. Examples

Several examples of realistic cavities will show the powerful applicability of URMEL. The accuracy is checked by comparing computed results with pill box solutions and spherical modes.

6.1. Accuracy

The first example is used to demonstrate the typical accuracy that one can expect from URMEL. Pill box solutions are not really the proper way to check the accuracy for transverse modes since they do not require the full system of the two matrices as mentioned earlier. Nevertheless it is convincing to see that the quadratic convergence is observed as:

$$|\Delta f| = \mathcal{O}(\Delta r \cdot \Delta z) = \mathcal{O}(1/N). \tag{23}$$

Table 1
Lowest transverse mode frequencies in a pill box of radius 1 m and gap length 1 m

Mode	Mesh	Comp. f/Mhz	Anal. f/Mhz	Error
TM110	11×11	182.18	182.82	-3.5×10^{-3}
	21×21	182.66		-8.8×10^{-4}
	31×31	182.75		-3.8×10^{-4}
	41×41	182.78		-2.2×10^{-4}
TE110	41×41	173.68	173.74	$+3.5\times10^{-4}$

Some results for the lowest transverse modes in a pill box (radius = 1 m, gap length = 1 m) are compared with analytical solutions in table 1.

Fig. 9 shows the relative error in frequency for various mesh sizes. The relative error $\Delta f/f_0$ - with f_0 as the lowest mode frequency - fits quite well to the relation

$$|\Delta f/f_0| \sim 1/(3.5\cdot N), \qquad N = \text{number of mesh points.} \tag{24}$$

More illuminating are the modes in a sphere since they also invoke the additional error which results from the limited accuracy in the shape approximation. Some comparisons show that the relative error caused by the approximated boundary exceeds the discretization error by roughly a factor of five, i.e. the discretization error becomes less important. Some comparisons are summarized in table 2. For mode notation see e.g. [21] and section 6.2.

6.2. *PETRA accelerating cavity*

Since most of the accelerating cavities are symmetric to a mid plane in longitudinal direction it is convenient to identify modes by the boundary condition on both sides of the structure. "E" denotes an electric boundary condition, i.e. the tangential electric field vanishes and "M" stands correspondingly for magnetic boundary condition. According to this definition there exist four different groups of modes in a single cavity cell: EE, EM, ME and MM. For further identification the azimuthal mode number is added. In each sub group modes are ordered with ascending frequency. EE2-5 is thus the fifth quadrupole mode found with electric boundary condition on both sides.

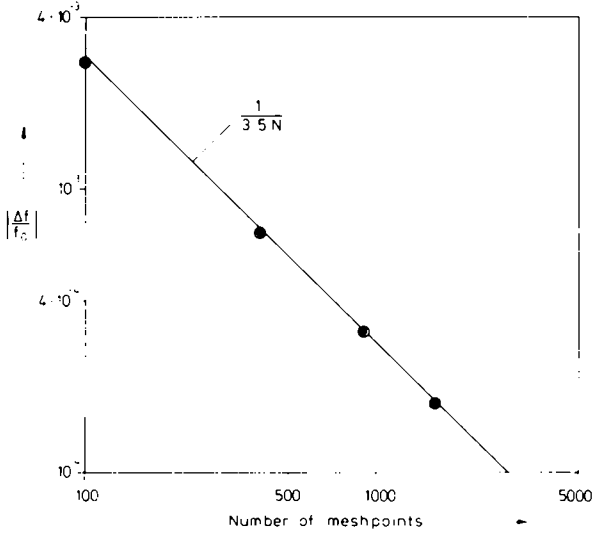

Fig. 9. Relative frequency error (computed) versus number of mesh points. The line represents the fit to $\Delta f = 1/3.5N$.

Table 2
Lowest modes found in a spherical cavity of radius 1 m. Due to the spherical symmetry the mode E11 can be calculated in cylindrical coordinates as TM0-EE-1 and as ME1-1 as well.

Mode	Mesh	f/Mhz	$\Delta f/f$	Q	$\Delta Q/Q$
E11	anal.	130.9	0.0	127136	0.0
TM0-EE-1	11×11	129.0	-1.5×10^{-2}	116212	-8.6×10^{-2}
	21×21	130.6	-2.3×10^{-3}	117516	-7.6×10^{-2}
	31×31	130.7	-1.5×10^{-3}	118529	6.8×10^{-2}
	41×41	130.8	-7.6×10^{-4}	118393	6.9×10^{-2}
ME1-1	11×11	130.2	-5.3×10^{-3}	127395	-2.0×10^{-3}
	21×21	131.4	-3.8×10^{-3}	134285	-5.6×10^{-2}
	31×31	131.3	-3.1×10^{-3}	134789	-6.0×10^{-2}
	41×41	131.1	-1.5×10^{-3}	138115	-8.6×10^{-2}

We will first present some results for the accelerating cavity in PETRA [22] the shape of which has been shown in figs. 1 and 2 together with a variable mesh. Fig. 10 shows the electric field at the plane $\varphi = 0°$ of the lowest dipole mode EE1-1 represented by little arrows the length of which is proportional to the field strength. The usual quantity displayed is $r \cdot H_\varphi$ in this case of monopole modes. For the first mode a contour plot is shown in fig. 11. Comparison of figs. 10 and 11 shows very clearly that the equipotential lines do *not* represent the direction of the actual field. Near the nose cone the lines turn around perpendicular to the electric field. A similar discouraging picture yields the contour plot of $r \cdot E_\varphi$ in the plane $\varphi = 90°$. The equipotential lines can hardly be interpreted as field lines of $\boldsymbol{H}$, see comparative figs. 12 and 13. As a conclusion we have to use arrow plots for *all* fields with azimuthal dependence. URMEL normally plots an arrow in the middle of each mesh cell. The *varying density* coming from the varying mesh step size can be sometimes misleading and it should be noticed that only the *length* of the arrows represents the field strength.

Figs. 14–17 show a few more transverse modes found in the PETRA cavity and table 3 summarizes the

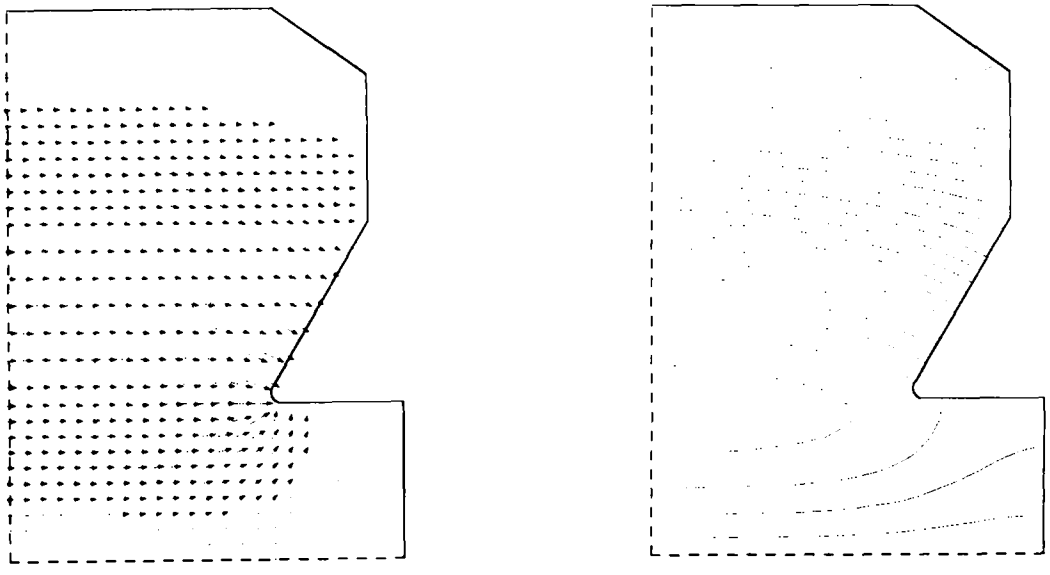

Fig. 10. Electric field at $\varphi = 0°$ of the lowest dipole mode found in the PETRA cavity *Note*: the *length* of the arrows is proportional to the field strength and not the density.

Fig. 11. Contour plot of $r \cdot H_\varphi$ at $\varphi = 0°$ for the lowest dipole mode in the PETRA cavity. The corresponding electric field is shown in fig. 10. *Note:* these contour lines *do not* give the direction of the electric field.

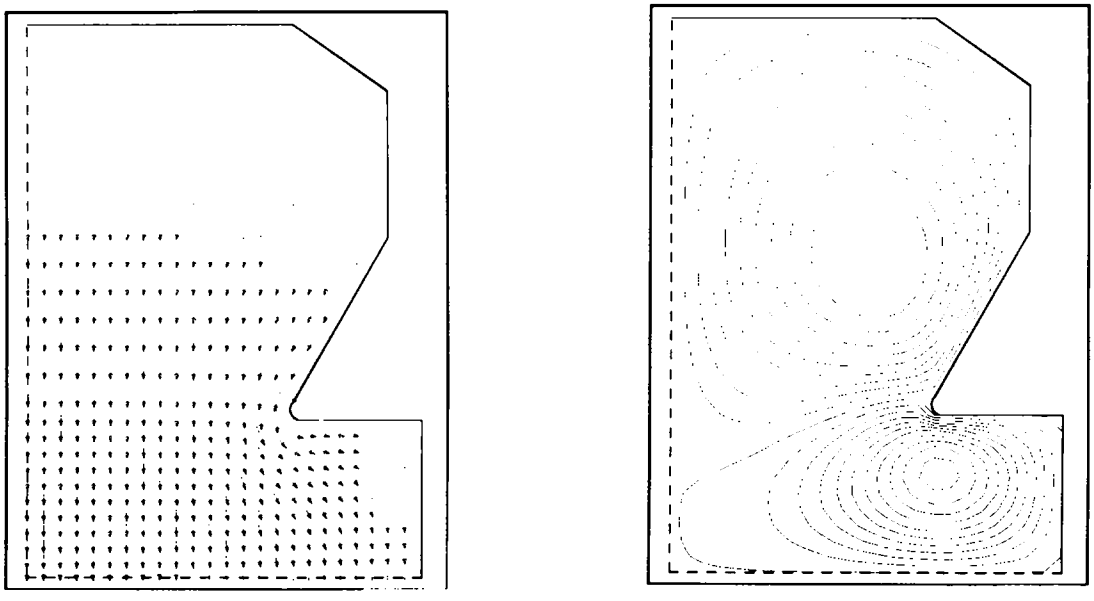

Fig. 12. Magnetic field at $\varphi = 90°$ of the lowest dipole mode found in the PETRA cavity.

Fig. 13. Contour plot of $r \cdot E_\varphi$ at $\varphi = 90°$ for the lowest dipole mode in the PETRA cavity. The corresponding magnetic field is shown in fig. 12. *Note*: these contour lines *do not* give the direction of the magnetic field.

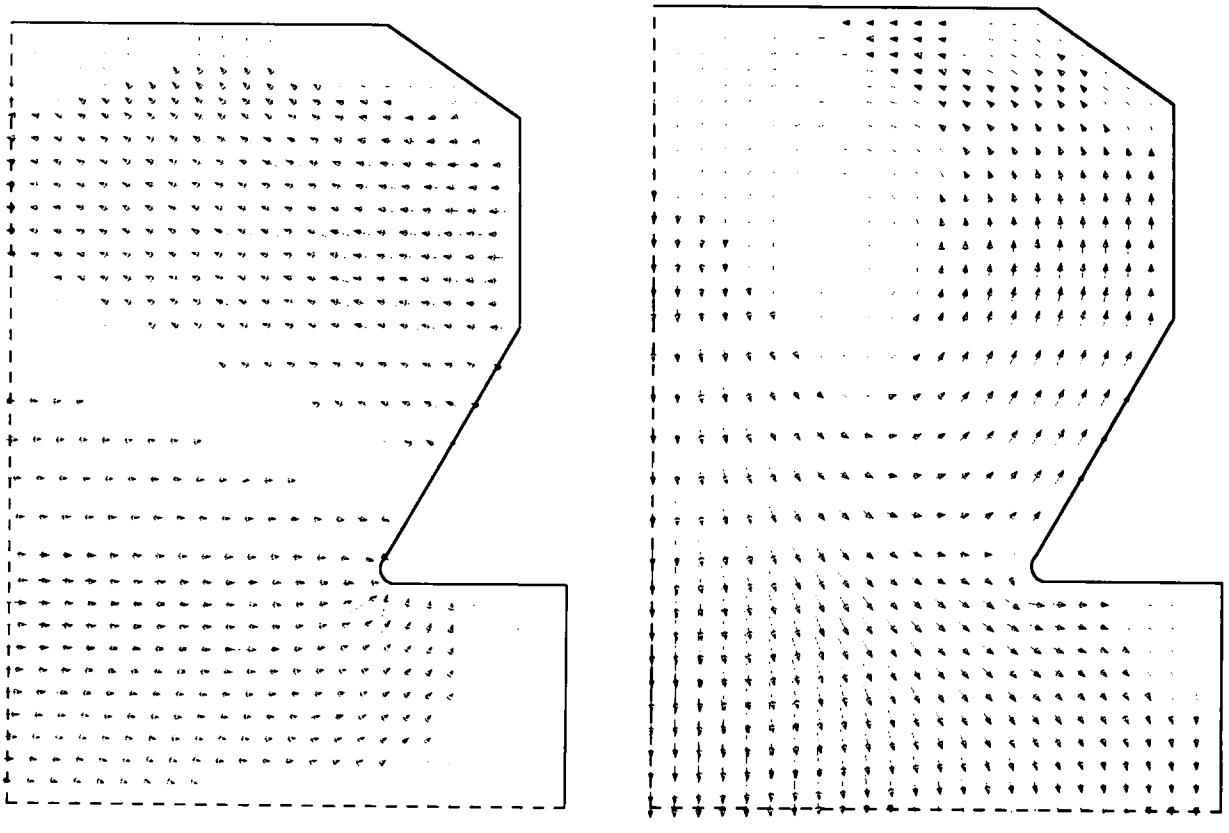

Fig. 14. Electric field of dipole mode EE1-4 in the PETRA cavity at $\varphi = 0°$.

Fig. 15. Magnetic field of dipole mode EE1-4 in the PETRA cavity at $\varphi = 90°$.

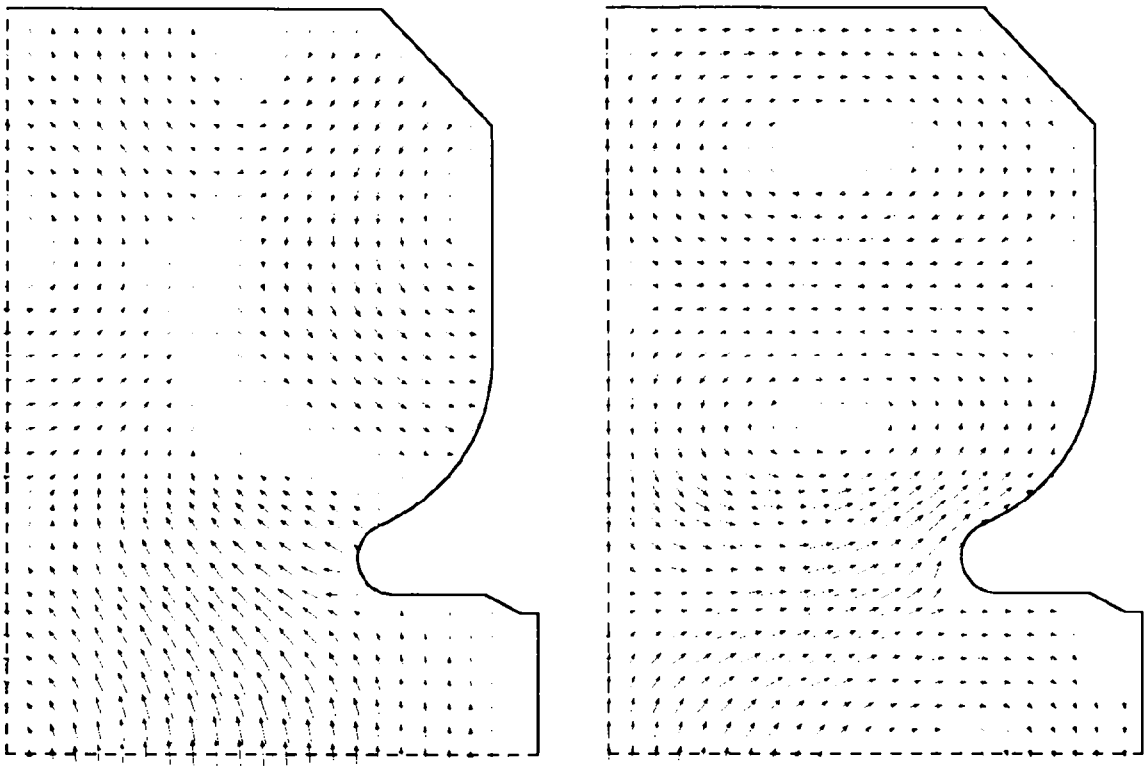

Fig. 16. Electric field of dipole mode EE1-8 in the new 7-cell PETRA cavity at $\varphi = 0°$.

Fig. 17. Magnetic field of dipole mode EE1-8 in the new 7-cell PETRA cavity at $\varphi = 90°$.

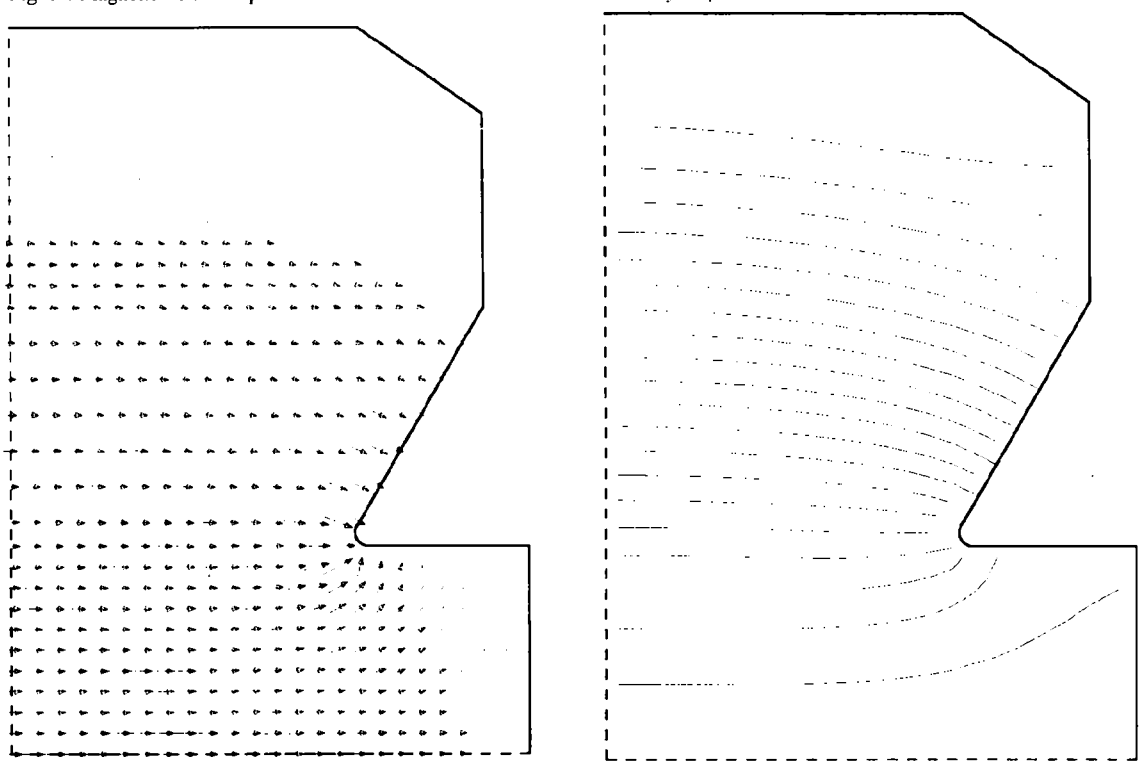

Fig. 18. Electric field of monopole mode TM0-EE-01 in the PETRA cavity.

Fig. 19. Contour plot of $r \cdot H_\varphi$ at $\varphi = 0°$ for the lowest TM monopole mode in the PETRA cavity. The corresponding electric field is shown in fig. 18. *Note*: these contour lines *do* give the direction of the electric field but their density is *not* proportional to the field strength.

Table 3
Lowest modes found the PETRA accelerating cavity (single cell)

Mode type	f/Mhz	Q	$R/Q/\Omega$/m	
TM0-EE-1	515.2	38624	107.6	monopole
TM0-EE-2	1247.2	42574	3.4	
TM0-EE-3	1287.4	70859	0.1	
TM0-EE-4	1826.1	49216	8.6	
TM0-EM-1	515.6	38655	103.1	
TM0-EM-2	1266.6	61612	4.8	
TM0-EM-3	1271.2	47260	0.0	
TM0-EM-4	1829.9	48753	7.6	
TM0-ME-1	756.5	33175	25.6	
TM0-ME-2	1471.0	48567	9.0	
TM0-ME-3	1749.6	47453	0.3	
TM0-ME-4	2043.2	53759	34.8	
TM0-MM-1	757.0	33171	19.6	
TM0-MM-2	1477.1	48726	15.6	
TM0-MM-3	1750.7	47974	1.5	
TM0-MM-4	2126.1	70830	0.0	
EE1-1	855.1	55821	22.5	dipole
EE1-2	1252.7	48008	0.4	
EE1-3	1446.0	58569	11.8	
EE1-4	1585.6	68668	0.1	
EE1-5	1669.4	90833	0.3	
ME1-1	732.3	43407	0.3	
ME1-2	1038.9	47065	41.3	
ME1-3	1338.7	96767	0.3	
ME1-4	1641.2	43652	8.1	
ME1-5	1771.9	56738	0.6	
EE2-1	1182.8	70995	0.4	quadrupole
EE2-2	1349.8	48826	0.1	
EE2-3	1708.2	60605	4.6	
EE2-4	1884.4	67608	5.6	
ME2-1	907.8	46684	0.1	
ME2-2	1353.1	54555	7.9	
ME2-3	1637.3	104626	0.0	
ME2-4	1812.4	45740	0.1	

results including the longitudinal modes. Figs. 18–21 finally show some lower longitudinal modes for which the usual equipotential lines of $r \cdot H_\varphi$ are shown as well as arrow plots. It can be easily seen that the equipotential lines do show the *direction* of the electric field and that their *density* is *not* proportional to the field strength but proportional to r times the field strength, see fig. 18–21.

6.3. Elliptical superconducting PETRA cavity

In storage rings with superconducting cavities a knowledge of mode structures is much more important than in normal conducting ones since some modes, must be damped by antennae for stability and cooling reasons. Figs. 22–25 show the lowest accelerating and deflecting modes found for the superconducting cavity [23] with which it is planned to convert PETRA into a 30 GeV storage ring [24]. Table 4 gives some measured modes [25] in comparison with computed results. The difference between the measured and calculated results is partly due to the fact the during the measurements a cutoff pipe of 20 cm length has been used whereas the side tube in the calculation is only 7.5 cm in order to save computation time.

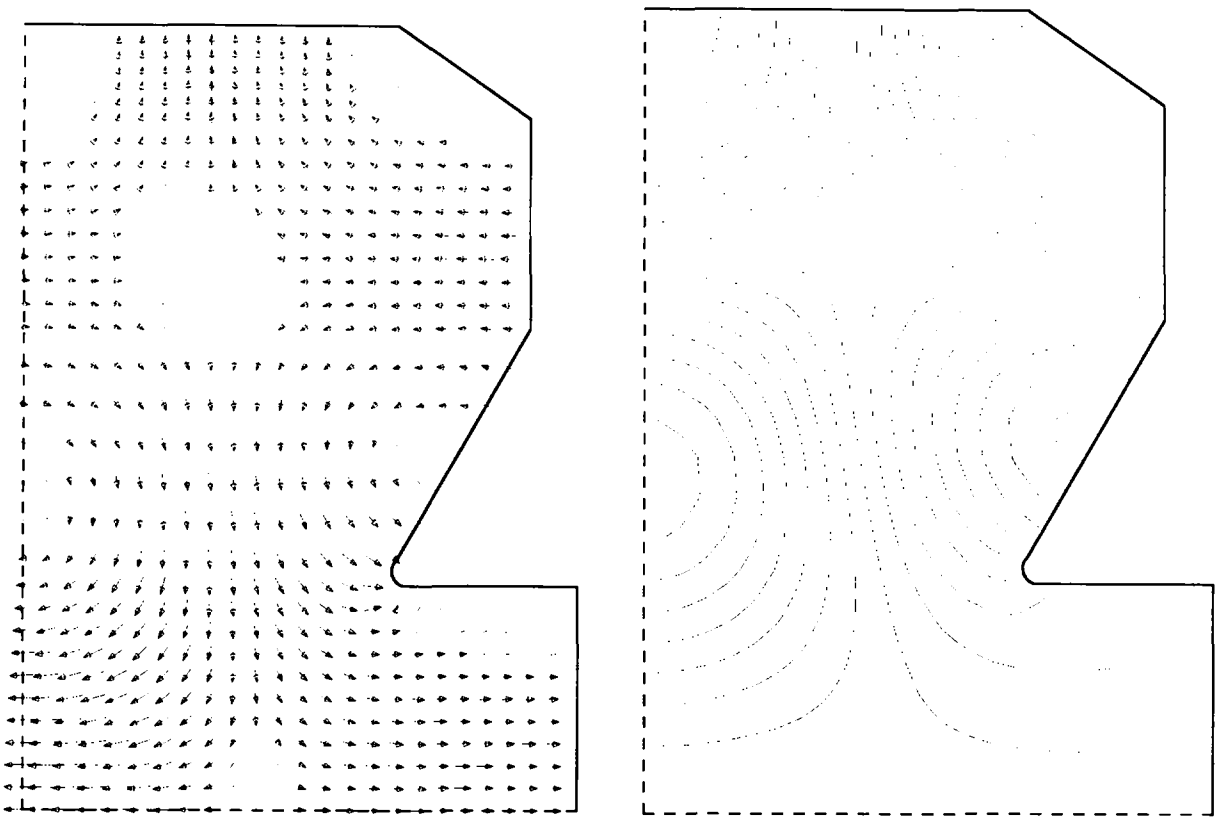

Fig. 20. Electric field of monopole mode TM0-EE-4 in the PETRA cavity.

Fig. 21. Contour plot of $r \cdot H_\varphi$ at $\varphi = 0°$ for the monopole mode TM0-EE-4 in the PETRA cavity. The corresponding electric field is shown in fig. 20.

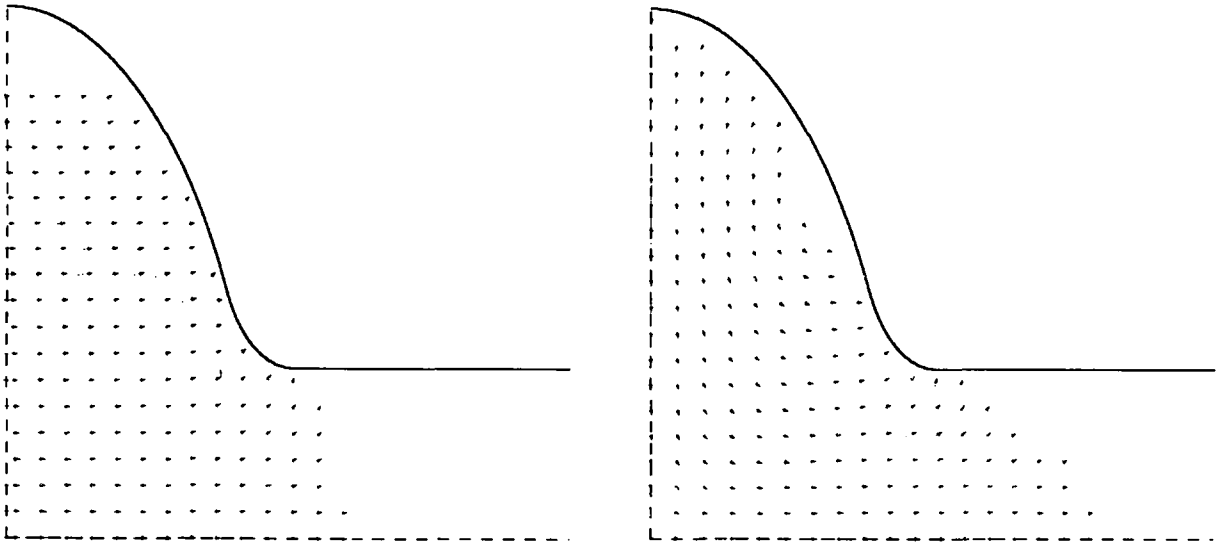

Fig. 22. Electric field of the accelerating monopole mode TM0-EE-1 (TM010) in the elliptical superconducting PETRA cavity.

Fig. 23. Electric field of monopole mode TM0-ME-1 (TM011) in the elliptical superconducting PETRA cavity.

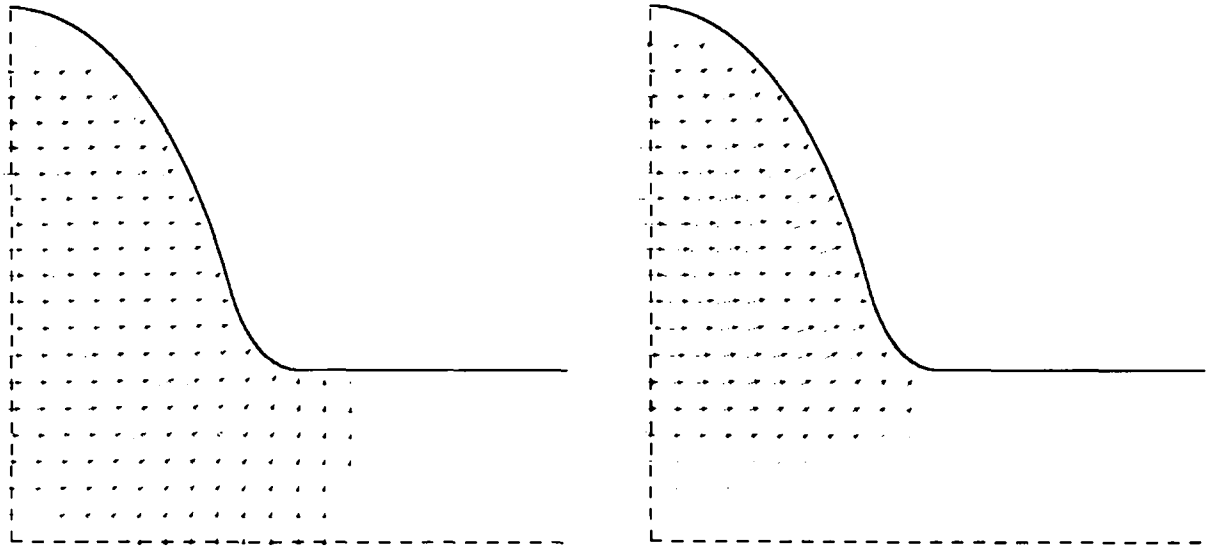

Fig. 24. Electric field of dipole mode EE1-1 in the elliptical superconducting PETRA cavity at $\varphi = 0°$.

Fig. 25. Electric field of quadrupole mode EE2-1 in the elliptical superconducting PETRA cavity at $\varphi = 0°$.

Table 4
Comparison between computed and measured modes in the elliptical superconductiong PETRA cavity

Mode	f/Mhz	Computed $R/Q/\Omega$/m	Q	f/Mhz	Measured $R/Q/\Omega$/m	Q
TM0-EE-1	988.5	762.0	29153	991.8	763.0	29200
ME-1-1	1358.9	124.0	37938	1359.9	-	-
EE-1-1	1398.1	307.0	32140	1404.2	-	-
ME-2-1	1838.9	29.0	43049	1837.6	-	-
EE-2-1	1858.7	27.0	37738	-	-	-
TM0-ME-1	1965.5	195.0	34659	1967.4	-	-
EE-1-2	2010.9	84.0	35258	2014.0	-	-
TM0-EE-2	2015.5	0.2	42652	2026.0	-	-

The author wishes to express his thanks to R.K. Cooper from Los Alamos National Laboratory for his continuing interest and support during the time when URMEL was coded at Los Alamos.

Appendix

In order to set up the two final difference operator eqs. (5) and (6) we have to deal with ten separate integrals of Maxwell's equations. The coupling differential equations (3) and (4) between $\boldsymbol{E}$ and $\boldsymbol{H}$ will be solved separately for each component. Boundary conditions and triangularly filled sub-cells are taken care of in these equations rather than in the final difference equation. This is the only manageable way to deal with 15625 different analytical forms for each of the eqs. (5) and (6). This sizeable number is due to the fact that each cell may be filled with four types of triangles, i.e. there are five ways to fill a mesh cell with material. Each type of filling is named with a number M_k, k being the running index of the cells. Fig. 26 shows the definitions. The type of filling of the six cells has an effect on the final form of (5) or (6) so there exist 5^6 possibilities. This is the price one has to pay for the advantage of a much better approximation

using triangularly filled cells. Since – as will be shown next – never more than four cells have an impact on equations of type (3) and (4) and since in most cases it is only two, the enormous number of 15625 possibilities is reduced to basically 25. This is certainly a number low enough to be programmable on a computer.

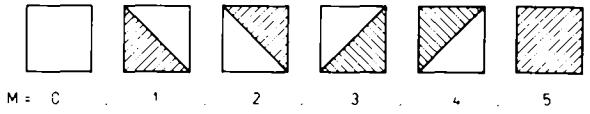

Fig. 26. Definition of the filling index M_k.

The derivation of the equations including the variable step sizes would invoke an enormous number of indices and variables. Since the basic principle can also be explained whith equal steps of length Δ in r and z we will restrict the following equations to this case. (This restriction concerns only this appendix and not the computer code.) The first equation is derived for the $E_{z,k}$ component.

Integration for E_z

Integrating the z component of rot $\boldsymbol{H} = k\boldsymbol{E}$ up to first order approximation yields the following linear relation, see fig. 27:

$$E_{z,k} = a_1 H_{\varphi,k} - a_2 H_{\varphi,k-J} - m a_3 H_{r,k}. \tag{A.1}$$

The formal coefficients $a_{1,2,3}$ are defined such that they are always positive. The FIT method is much easier to understand when applied to Maxwell's equations in integral form:

$$\oint \boldsymbol{H} \cdot \mathrm{d}\boldsymbol{s} = k \int \boldsymbol{E} \cdot \mathrm{d}\boldsymbol{A}. \tag{A.2}$$

Integrating (A.2) over the area shown in fig. 27 and around the circumference of the area from $\varphi = 0$ to $\varphi = \psi$ yields:

$$kE_{z,k}(i-1)\Delta^2 \int \cos m\varphi \mathrm{d}\varphi = H_{\varphi,k}(i-\tfrac{1}{2})\Delta \int \cos m\varphi \mathrm{d}\varphi$$

$$- H_{\varphi,k-J}(i-\tfrac{3}{2})\Delta \int \cos m\varphi \mathrm{d}\varphi - H_{r,k}\Delta \sin m\psi. \tag{A.3}$$

Note that all integrals over φ in the following extend from 0 to ψ. This equations must be valid for any ψ and thus can be written as:

$$\Delta k E_{z,k} = [(2i-1)/(2i-2)]\, H_{\varphi,k} - [(2i-3)/(2i-2)]\, H_{\varphi,k-J} - [m/(i-1)]\, H_{r,k}. \tag{A.4}$$

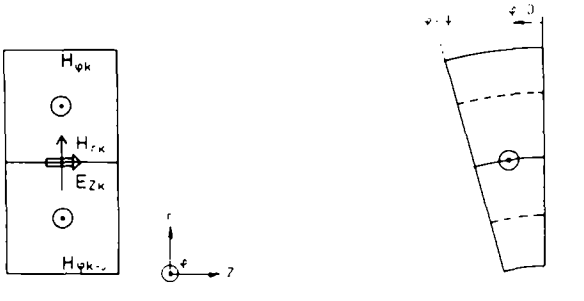

Fig. 27. Area of integration for $E_{z,k}$.

Table 5
Logical table for integration $E_{z,k}$

M_k		M_{k-J}	a_1	a_2	a_3
$(1 \vee 3 \vee 5)$	$\wedge$	$(2 \vee 4 \vee 5)$	0	0	0
$(2 \vee 4 \vee 0)$	$\wedge$	$(1 \vee 3 \vee 0)$	$[(2i-1)/(2i-2)]$	$[(2i-3)/(2i-2)]$	$1/(i-1)$

Boundary conditions may change this equation. If cell number k or cell number $k-J$ is filled with infinitely conducting metal such that $E_{z,k}$ is zero then equation (A.4) is not needed and all coefficients are set to zero. The coefficients may be put into a logical table (see table 5). This logical table is obviously easy to verify in a computer.

Integration for H_φ

In order to replace the H_φ components in the above equation (A.4) we have to solve the second Maxwell's equation in integral form:

$$\oint \boldsymbol{E} \cdot \mathrm{d}\boldsymbol{s} = k \int \boldsymbol{H} \cdot \mathrm{d}\boldsymbol{A}. \tag{A.5}$$

The area of integration is simply a mesh cell in the (r, z) plane as shown in fig. 28. Considering a cell which is not filled with any material we get simply:

$$k\Delta^2 H_{\varphi,k} = \Delta E_{z,k} - \Delta E_{z,k+J} + \Delta E_{r,k+1} - \Delta E_{r,k}. \tag{A.6}$$

In general there exist five ways in which the cell may be filled with metal and in these cases the above equation will have to be changed. If the cell is filled with a triangle the area of integration is halved, two coefficients are doubled and two vanish. We introduce formal coefficients:

$$\Delta k H_{\varphi,k} = b_1 E_{z,k} - b_2 E_{z,k+J} + b_3 E_{r,k+1} - b_4 E_{r,k}. \tag{A.7}$$

Table 6 gives all the possible combinations for the b's:
By means of the above equations we are now able to eliminate $H_{\varphi,k}$ from eq. (A.4). In order to eliminate the second azimuthal magnetic field component, a second table very similiar to the above one has to be written for the formal coefficients $c_{1,2,3,4}$:

$$\Delta k H_{\varphi,k-J} = c_1 E_{z,k-J} - c_2 E_{z,k} + c_3 E_{r,k-J+1} - c_4 E_{r,k-J}. \tag{A.8}$$

Integration for H_r

$H_{r,k}$ is the last component left to be eliminated from eq. (A.4) Fig. 29 shows a suitable area for

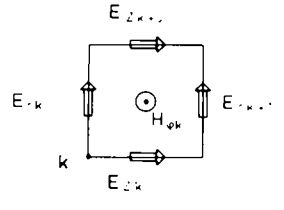

Fig. 28. Area of integration for $H_{\varphi,k}$

Table 6
Logical table for integration H_φ

M_k	b_1	b_2	b_3	b_4
0	1	1	1	1
1	0	2	2	0
2	2	0	0	2
3	0	2	0	2
4	2	0	2	0
5	0	0	0	0

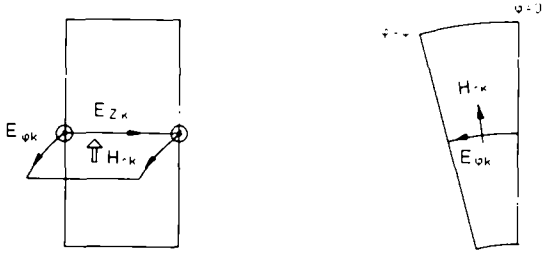

Fig. 29. Area of integration for $H_{r,k}$.

integrating equation (A.4):

$$H_{r,k}(i-1)\Delta^2 k\int \sin m\varphi \mathrm{d}\varphi = E_{\varphi,k}(i-1)\Delta\int \sin m\varphi \mathrm{d}\varphi$$

$$- E_{\varphi,i-1}(i-1)\Delta\int \sin m\varphi \mathrm{d}\varphi - E_{z,k}\Delta + E_{z,k}\Delta\cos m\psi \qquad \text{(A.9)}$$

For the formal coefficients:

$$\Delta k H_{r,k} = -d_1 m E_{z,k} + d_2 E_{\varphi,k} - d_3 E_{\varphi,k+1} \qquad \text{(A.10)}$$

we get table 7:
Combining eqs. (A.1), (A.7), (A.8) and (A.10) enables a replacement of all magnetic field components in (A.1) by electric ones:

$$(\Delta k)^2 E_{z,k} = (a_1 b_1 + a_2 c_2 + a_3 d_1 m^2) E_{z,k} - a_1 b_2 E_{z,k+J} - a_2 c_1 E_{z,k-J} + a_1 b_3 E_{r,k+1}$$
$$- a_1 b_4 E_{r,k} - a_2 c_3 E_{r,k-J+1} + a_2 c_4 E_{r,k\ \ J} - m a_3 d_2 E_{\varphi,k} + m a_3 d_3 E_{\varphi,k+1}. \qquad \text{(A.11)}$$

There are still some components that can be eliminated from the above equation thus reducing the total number of unknown quantities. The third Maxwell's equation yields such a relation between electric field

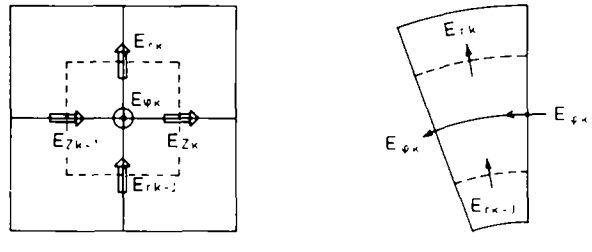

Fig. 30. Area of integration of $\boldsymbol{E}$ over volume surface.

Table 7
Logical table for integration H_r

M_k		M_{k-J}	d_1	d_2	d_3
$(1\vee 3\vee 5)\ \wedge$	$(2\vee 4\vee 5)$	0	0	0	
$(0\vee 2\vee 4)\ \wedge$	$(1\vee 3\vee 0)$	$1/(i-1)$	1	1	

components only:

$$\oint \boldsymbol{E}\cdot \mathrm{d}\boldsymbol{A} = 0. \tag{A.12}$$

This equation is automatically fulfilled in the FIT [17] method and can be used to eliminate one of the three electric field components by means of integration over the area shown in fig. 30. With the same approximations as used in the previous integrations we get the following relation between the electric field components located around a mesh node with number k:

$$0 = E_{\varphi,k}\Delta^2 \sin m\psi + E_{r,k}\left(i-\tfrac{1}{2}\right)\Delta^2 \int \cos m\varphi \mathrm{d}\varphi - E_{r,k-J}\left(i-\tfrac{3}{2}\right)\Delta^2 \int \cos m\varphi \mathrm{d}\varphi$$

$$+ E_{z,k}(i-1)\Delta^2 \int \cos m\varphi \mathrm{d}\varphi - E_{z,k-1}(i-1)\Delta^2 \int \cos m\varphi \mathrm{d}\varphi \tag{A.13}$$

Using the formal coefficients:

$$mE_{\varphi,k} = e_1 E_{r,k-J} - e_2 E_{r,k} + e_3 E_{z,k-1} - e_4 E_{z,k} \tag{A.14}$$

we could set up a table with essentially only two answers. If $E_{\varphi,k}$ does vanish due to a metallic filling in one of the four neighbouring cells all coefficients are zero. In all other cases the coefficients in eq. (A.13) do not change. In order to eliminate the second E_φ component in eq. (A.11) we need one more table for:

$$mE_{\varphi,k+1} = f_1 E_{r,k-J+1} - f_2 E_{r,k+1} + f_3 E_{z,k} - f_4 E_{z,k+1}. \tag{A.15}$$

Finally we get an equation which relates only E_z with E_z and E_r:

$$\begin{aligned}(\Delta k)^2 E_{z,k} = {} & \left(a_1 b_1 + a_2 c_2 + a_3 d_1 m^2 + a_3 d_2 e_4 + a_3 d_3 f_3\right) E_{z,k} \\ & - a_1 b_2 E_{z,k+J} - a_2 c_1 E_{z,k-J} - a_3 d_2 e_3 E_{z,k-1} - a_3 d_3 f_4 E_{z,k+1} \\ & + \left(a_2 c_4 - a_3 d_2 e_1\right) E_{r,k-J} - \left(a_2 c_3 - a_3 d_3 f_1\right) E_{r,k-J+1} \\ & - \left(a_1 b_4 - a_3 d_2 e_2\right) E_{r,k} + \left(a_1 b_3 - a_3 d_3 f_2\right) E_{r,k+1}.\end{aligned} \tag{A.16}$$

The above difference equation connects the central $E_{z,k}$ component with four neighbours of E_z and E_r as shown schematically in fig. 4.

In many cavity calculations it is advantageous to enable the use of a boundary condition of an infinitely permeable wall. Some of the above equations have to be changed when such a boundary is present but this would invoke too many details to be explained here. Similarly to the above procedure of eliminating components so that only two types remain, one can deduce a corresponding equation for $E_{r,k}$ which connects $E_{r,k}$ only with E_r and E_z as shown schematically in fig. 4.

List of symbols

$\boldsymbol{E}$, $\boldsymbol{H}$	electric and magnetic field
$E_{r,k}$	radial electric field component at mesh node k
$H_{\varphi,k}$	azimuthal magnetic field component at node k
Z_0, Y_0	free space impedance, admittance
m	azimuthal mode number, i.e. fields $\propto \cos/\sin m\varphi$

EE1-4	mode with electric boundary on both sides, dipole, 4th mode found in this subset
ME2-3	mode with magnetic boundary on the left and electric boundary on the right, quadrupole, third mode found in this subset
k	wave number, $k = \omega/c$
i, j	running index for mesh lines in r, z direction
I, J	number of mesh lines in r, z direction
k	as index: node number $k = (i-1)\cdot I + j$
a_k	quantity a belongs to mesh node k
$O(h)$	Landau symbol
A	matrix for monopole modes
A_{rr}	submatrix connecting E_r and E_r for transverse modes
$\boldsymbol{u}_j$, $\boldsymbol{v}_i$	iterated right/lefthand side eigenvectors'
A^t	transposed matrix A
$a_{rr,k,p}$	element of A_{rr} where p is 0–4 denoting one of the diagonals
$\boldsymbol{e}$	column vector holding all unknown radial and longitudinal electric field components
$\boldsymbol{h}$	column vector holding all unknown azimuthal magnetic field components
R/Q	geometric impedance, (power law: $P = U^2/(2\cdot R)$). The voltage U is taken at $r =$ beam tube radius for transverse modes.
Q	quality factor
$\boldsymbol{e}_{r,\varphi,z}$	unit vector in r, φ, z direction
R	domain of real numbers
R^N	vector space of dimension N upon R
$R^{N\times N}$	set of $N \times N$ matrices upon R
λ	eigenvalue
$\in$	element of.

References

[1] M. Albani and M. Bernardi IEEE MTT22 (1974) 446.
[2] W. Wilhelm, Part. Accel. 12 (1982) 139.
[3] Z.J. Csendes and R.M.J. Silvester, IEEE MTT18 (1970) 1124.
[4] J.S. Hornsby and A. Gopinath, IEEE MTT17 (1969) 684–690.
[5] S. Akhtarazad and P.B. Johns, IEE 122 (12) (1975) 1344–1348 and 1349–1352.
[6] T. Weiland, Electronics and Communication (AEU) 33 (1979) 170.
[7] H.C. Hoyt, D.D. Simmonds and W.F. Rich, Rev. Sci. Instr. 37 (1966) 755.
[8] K. Halbach and R.F. Holsinger, Part. Accel. 7 (1976) 213.
[9] T. Weiland, Cavity mode computer code CAVO, CERN (ISR-TH) 1980, unpublished.
[10] B.B. Fomel, U.P. Jackolew, M.M. Karliner and P.B. Lysansky, Part. Accel. 11 (1981) 173.
[11] P. Fernandes and R. Parodi, Part. Accel. 12 (1982) 131–138.
[12] K. Bane and B. Zotter, Proc. XIth Internat. Conf. on High Energy Accel. Geneva (Birkhauser Verlag, 1980) pp. 581.
[13] E. Keil, Nucl. Instr. and Meth. 100 (1972) pp. 419.
[14] R.L. Gluckstern, R.F. Holsinger, K. Halbach and G.N. Minerbo, Proc. 1981 Linear Accel. Conf., Santa Fe, New Mexico.
[15] A.G. Daikovskii, Iu.I. Portugalev and A.D. Riabov, Instit. for High Energy Physics Sherpukov 1980 IFVE80-107 translated: LA-TR-82-22 Los Alamos Scientific Lab., Los Alamos, New Mexico.
[16] R.L. Gluckstern and R.K. Cooper, private communication.
[17] T. Weiland, Electron. and Communic. (AEU) 31 (1977) 116.
[18] T. Weiland, Proc. XIth Internat. Conf. on High Energy Accel., Geneva (1980) pp. 575.
[19] T. Weiland, DESY M-82-24 (October 1982).
[20] E. Isaacson and H.B. Keller, Analyse numerischer Verfahren (Verlag Harri Deutsch, Zurich Frankfurt, 1973).
[21] H. Henke, CERN (ISR-RF)81-29 (August 1981).
[22] PETRA proposal, DESY (Feb. 1976).
[23] DESY drawing #0-81-8180/A. 100 (1981).
[24] T. Weiland, DESY M-82-02 (Feb. 1982).
[25] J. Peters, private communication and DESY M-83-# #, to be published.